ACES Asian Chemical Editorial Society

DOI: 10.1002/asia.202000467

CHEMISTRY AN ASIAN JOURNAL Full Paper

Special Collection

Hierarchical Equations of Motion Simulation of Temperature-Dependent Two-Dimensional Electronic Spectroscopy of the Chlorophyll *a* Manifold in LHCII

Xuan Leng,[a] Thanh Nhut Do,[a] Parveen Akhtar,[a, b, c] Hoang Long Nguyen,[a] Petar H. Lambrev,*[b] and Howe-Siang Tan*[a]

Abstract: We simulated two-dimensional electronic spectra (2DES) of the chlorophyll *a* manifold of light-harvesting complex II (LHCII) at various temperatures (77, 110, 150, 190, 230, 273, and 293 K) using the hierarchical equations of the motion-phase matching approach. We confirm the main excitation energy transfer pathways assignments within the chlorophyll *a* manifold of LHCII measured in a recent work (J. Phys. Chem. B 2019, 123, 6765–6775). The calculated transfer rates are also in general agreement with the measured rates. We also provided theoretical confirmation for the experimental assignments, as uphill and downhill energy transfer processes, of 2D spectral features that were reported in recent experimental reports. These temperature-dependent features were also ascertained to follow the detailed-balance principle.

Introduction

Light-harvesting complexes are essential for photosynthesis. They absorb sunlight and transfer energy to the reaction center through excitation energy transfer (EET) where charge separation is initiated.[1] In higher plants, the light-harvesting complex II (LHCII) is the primary antenna and is also the most abundant membrane protein-pigment complex on Earth.[2] It is a trimeric system where each monomer is comprised of eight chlorophyll *a* (Chl *a*) molecules, six chlorophyll *b* (Chl *b*) molecules and four carotenoids (Cars).[3,4] The dynamics of EET between Chls in LHCII has been studied by various time-resolved spectroscopies,[5–8] such as transient absorption, time-resolved fluorescence and three-pulse photon echo peak shift spectroscopy. In comparison to these time-resolved spectroscopies, two-dimensional electronic spectroscopy (2DES) provides an extra dimension for studying the EET dynamics in molecular aggregates in which the excitation frequency is resolved.[9] Since the first 2DES experiment was demonstrated about two decades ago,[10] it has been widely used to study the ultrafast phenomena in a variety of photosynthetic systems.[11–19] This field has garnered much interest and debate, in particular regarding whether the EET processes rely on quantum or classical mechanisms.[20,21]

The EET process in LHCII has also been investigated using 2DES at both cryogenic and ambient temperatures. These studies include the 2DES of LHCII performed at low temperature (77 K), in which fast EET dynamics (< 100 fs) were revealed.[22] 2DES experiments at ambient temperatures revealed different timescales, generally in agreement with transient absorption studies, identifying a long-lived 'bottleneck' state and pathways of EET.[23,24] The EET dynamics between Cars and Chls via a debated dark state was also observed by ultra-broadband 2DES.[25] The equilibration processes among Chls *a* at physiological temperature[26] and cryogenic temperatures[27] were elucidated using 2DES.

Chls in LHCII form a complex EET network connecting multiple excitonic states. The energy gaps between them are such that, at room temperature, thermally activated processes are expected to happen, leading to both downhill (high to low energy) and uphill (low to high energy) EET processes.[28] 2DES is suitable to study these complex energy equilibration processes due to its ability to resolve both the excitation and detection frequency axes.[24,26,27] To validate the assignments of features observed in the 2D electronic spectra to particular uphill and downhill EET pathways, it is essential to reproduce these features in theoretical simulations at various temperatures. Furthermore, a theoretical model of the spectroscopic data can provide deeper insights into the EET processes.[29–32] The hierarchical equations of motion (HEOM) is a type of non-perturbative, non-Markovian quantum dissipative method to calculate the EET dynamics.[33–37] It has been applied to simulate various types of spectroscopic signals by temporally propagating the reduced density matrix.[38–40] For a detailed simulation of 2D electronic spectra, the equation of motion-phase matching approach (EOM-PMA) can explicitly describe the effects of the finite laser pulses used in a 2DES experiment.[41–45] These two

[a] Dr. X. Leng, Dr. T. N. Do, Dr. P. Akhtar, H. L. Nguyen, Prof. H.-S. Tan
Division of Chemistry and Biological Chemistry, School of Physical and Mathematical Sciences
Nanyang Technological University
21 Nanyang Link, 637371 Singapore (Singapore)
E-mail: howesiang@ntu.edu.sg

[b] Dr. P. Akhtar, Dr. P. H. Lambrev
Biological Research Centre
Szeged, Temesvári körút 62, Szeged 6726 (Hungary)
E-mail: lambrev.petar@brc.hu

[c] Dr. P. Akhtar
ELI-ALPS, ELI-HU Nonprofit Ltd.
Wolfgang Sandner utca 3, Szeged 6728 (Hungary)

Supporting information for this article is available on the WWW under https://doi.org/10.1002/asia.202000467

This manuscript is part of a special collection for the 50th Anniversary of the Singapore National Institute of Chemistry.

methods have been combined to form HEOM-PMA which allows us to simulate the time-dependent 2D electronic spectra resulting from EET in the complex.[46–50]

Room temperature 2D spectra of LHCII have been simulated by EOM-PMA with the time-nonlocal quantum master equation[24] and HEOM.[48] Recent works showed that temperature-dependent protein dynamics of LHCII affect both excited-state energies and electron-phonon coupling.[51] In addition to the excited-state energy, the electron-phonon coupling mediates the EET dynamics in light-harvesting complexes by broadening the spectral range of light absorption.[52] Thus, comparing the simulated 2D spectra at low temperatures with the experimental data will provide insights into the changes in EET processes induced by the protein structure change of the light-harvesting complex. In this work, we theoretically explore the temperature-dependent EET processes in the Chl *a* manifold of LHCII by simulating the 2D electronic spectra with HEOM-PMA. Our main aim is 1) to examine the relationship between the simulated and the experimental spectra and dynamics using the HEOM-PMA approach and 2) to test the temperature dependence of the EET by only varying the temperature parameter without invoking changes in the system Hamiltonian or spectral density.

The article is arranged as follows. We first briefly describe the theoretical method to simulate the 2D electronic spectra at the various temperatures. We then present the results and discussions, and provide comparisons between the temperature dependent simulated and experimental data. Finally, conclusions are then made.

Computational Methods

Model Hamiltonian

The Hamiltonian H_{mol} of a light-harvesting complex system is considered as a Frenkel exciton model H_e with N two-level chromophores coupled to a phonon bath H_{ph}

$$H_{mol} = H_e + H_{ph} + H_{e-ph} \ . \tag{1}$$

The excitonic Hamiltonian H_e in the site representation is written as

$$H_e = \sum_{n=1}^{N} |n\rangle\langle n|\varepsilon_n + \sum_{m<n} V_{mn}(|m\rangle\langle n| + |n\rangle\langle m|) \ , \tag{2}$$

where N is the total number of the chromophores considered in the Hamiltonian, ε_n is the site energy of the nth chromophore, V_{mn} is the inter-chromophore electronic coupling, $|n\rangle$ describes a state where only the nth chromophore is excited. The excitonic Hamiltonian of the LHCII complex is the same as in a previous work,[48] in which the coupling constants between different pigments are obtained by point-dipole approximation constructed by Novoderezhkin et al.[29] with the site energies using an improved version by Duan et al.[24]

The Hamiltonian of the phonon degrees of freedom H_{ph} is given by a set of harmonic oscillators:

$$H_{ph} = \sum_{n=1}^{N} \sum_{i=1}^{N_b^n} \left(\frac{p_{ni}^2}{2} + \frac{1}{2}\omega_{ni}^2 x_{ni}^2 \right) \tag{3}$$

where N_b^n is the number of vibrational modes belonging to the n^{th} chromophore, x_{ni} and p_{ni} are the position and momentum of the i^{th} harmonic oscillator with frequency ω_{ni}. The electron-phonon coupling term H_{e-ph} causes site energy fluctuations that are independent of each chromophore

$$H_{e-ph} = \sum_{n=1}^{N} \sum_{i=1}^{N_b^n} c_{ni} x_{ni} |n\rangle\langle n| \tag{4}$$

The spectral density $J_n(\omega)$ is used to characterize electron-phonon interaction on the n^{th} chromophore, which is defined as

$$J_n(\omega) = \frac{\pi}{2} \sum_{i=1}^{N_b^n} \frac{c_{ni}^2}{\omega_{ni}} \delta(\omega - \omega_{ni}). \tag{5}$$

In this work, the spectral density is assumed to be the same for all chromophores and temperature independent. The Debye-type spectral density is used

$$J(\omega) = \frac{2\lambda_0 \gamma \omega}{\omega^2 + \gamma^2}, \tag{6}$$

where $\gamma^{-1} = 50$ fs is the bath relaxation time and $\lambda_0 = 50\ \text{cm}^{-1}$ is the reorganization energy reflecting the electron-phonon coupling strength.

Hierarchical equations of motion-phase matching approach (HEOM-PMA)

The HEOM-PMA method was used to simulate the 2D electronic spectra. The details of this method are described in Ref. [47–50]. Briefly, the total Hamiltonian is given by

$$H_{tot} = H_{mol} + H_{int} \tag{7}$$

where H_{mol} is the system Hamiltonian and H_{int} describes the interaction between the molecular system and the laser field

$$H_{int} = -\mu \cdot \boldsymbol{E}(t), \tag{8}$$

where μ is the total dipole operator expressed via the transition dipole moments of individual pigment molecules $\boldsymbol{d_n}$ according to the equation

$$\mu = \sum_{n=1}^{N} \boldsymbol{d}_n (|n\rangle\langle 0| + |0\rangle\langle n|) \tag{9}$$

The time-dependent electric field in Eq. (8) is described as

$$\boldsymbol{E}(t) = \sum_{m=1}^{3} \left[E_m(t - \tau_m) e^{-i(\omega_m t - \boldsymbol{k}_m \cdot \boldsymbol{r})} + c.c. \right] \boldsymbol{e}_m \tag{10}$$

where $E_m(t - \tau_m)$ is the laser pulse profile, ω_m is the frequency of the pulse, $\boldsymbol{k}_m$ is the wave vector, and $\boldsymbol{e}_m$ is the unit vector

representing the polarization of the electric field. $\tau_1 = \tau + T_w$, $\tau_2 = T_w$ and $\tau_3 = 0$ where τ and T are the interpulse delays between pulses 1 and 2, and pulses 2 and 3, respectively. In this work, a Gaussian function is used to represent the pulse profile as described in Ref. [48].

The temperature effect is described in the bath correlation function. In the HEOM formalism, the bath correlation function is written as a sum of exponential terms

$$C(t) = \sum_{k=0}^{\infty} c_k e^{-\gamma_k t} \tag{11}$$

For the Debye-type spectral density in Eq. (6), we have $\gamma_0 = \gamma$, $\gamma_k = 2k\pi/\beta \ (k \geq 1)$ corresponding to the Matsubara frequencies,[33–37]

$$c_0 = \lambda_0 \gamma \left[\cot\left(\frac{\beta\gamma}{2}\right) - i\right] \tag{12}$$

and

$$c_k = \frac{8k\pi\lambda_0\gamma}{(2k\pi)^2 - (\beta\gamma)^2}, \ k \geq 1, \tag{13}$$

where $\beta = 1/k_B T$, k_B is the Bolzmann constant and T is the absolute temperature.

The third-order polarization for the 2D rephasing signal in the $\boldsymbol{k}_s = -\boldsymbol{k}_1 + \boldsymbol{k}_2 + \boldsymbol{k}_3$ direction is calculated by propagating three auxiliary density matrices[41–44] $\rho_1(t)$, $\rho_2(t)$, and $\rho_3(t)$ using the HEOM method.[33–37] For the rephasing third-order polarization signal, $P^{(3)}_{rp}(t)$, we have

$$P^{(3)}_{rp}(t) = \langle \boldsymbol{X} \cdot \boldsymbol{e}_4 [\rho_1(t) - \rho_2(t) - \rho_3(t)] \rangle. \tag{14}$$

Here, $\langle \ldots \rangle$ denotes the average over the electronic degrees of freedom, $\boldsymbol{X} = \sum_{n=1}^{N} \boldsymbol{d}_n |0\rangle\langle n|$ is the de-excitation transition dipole and $\boldsymbol{e}_4$ represents the signal orientation, which is assumed to be the polarization vector of the local oscillator pulse. To calculate the third-order non-rephasing signal $P^{(3)}_{nrp}(t)$, we exchange the order of the first two laser pulses. $P^{(3)}_{rp}(t)$ and $P^{(3)}_{nrp}(t)$ are calculated for a series of interpulse delays τ and T_w and combined to give $P^{(3)}(\tau, t, T_w) = P^{(3)}_{rp}(\tau, t, T_w) + P^{(3)}_{nrp}(\tau, t, T_w)$. The real part of the double Fourier transform over τ and t of the total third-order polarization signal, $P^{(3)}(\tau, t, T_w)$ gives the 2D spectrum $S(\omega_\tau, \omega_t, T_w)$.[53,54] We perform the calculation to obtain simulated 2D spectra $S(\omega_\tau, \omega_t, T_w)$ for different waiting times range, (0 to 1), (1 to 5), (5 to 10), (10 to 20), (20 to 60) ps at 0.025, 0.5, 1, 2.5, 5 ps intervals, respectively. The simulated 2D spectra can then be compared with the experimental 2D spectra $S_{expt}(\omega_\tau, \omega_t, T_w)$ that have been reported in Akhtar et al.,[27] with T_w ranging from T_w = 100 fs to 100 ps in a quasilogarithmic progression.

Two-dimensional decay-associated spectra

Both the simulated and experimental time-dependent 2D spectra $S(\omega_\tau, \omega_t, T_w)$ are then subjected to a multidimensional global fitting routine and results in two-dimensional decay-associated spectra (2DDAS) that qualitatively reveal various EET pathways in the 2D spectra.[26,27,55] A series of 2D spectra $S(\omega_\tau, \omega_t, T_w)$ taken at different waiting time T_w are then fitted to the formula

$$S(\omega_\tau, \omega_t, T_w) = \sum_{i}^{n} A_i(\omega_\tau, \omega_t) e^{-\frac{T_w}{\tau_i}} \tag{15}$$

where n is the total number of lifetime components, $A_i(\omega_\tau, \omega_t)$ is the 2DDAS that decays exponentially with associated lifetime τ_i.

Results and Discussion

In this work, we focus on investigating EET in the Chl *a* manifold of LHCII while excluding the Chl *b* states from the calculations. For this reduced model, the spectral density used in the current simulation should be more reliable. This is due to the fact that high-frequency modes, which may affect EET between the Chl *a* and *b* manifolds,[22,32,56] do not need to be considered. The 2D electronic spectra are simulated from the reduced LHCII monomer model for different temperatures 77, 110, 150, 190, 230, 273, and 293 K (parts of the data are not shown). The static disorder is described by a Gaussian distribution with a FWHM of 120 cm^{-1} and is assumed to be the same for different pigments and temperature-independent. In the simulation, 200 averages over the static disorder in site energies and molecular orientations are included.

Figure 1 shows the calculated linear absorption spectrum of LHCII (dash red), which agrees well with the experimental results (open circles) at 298 K above 645 nm. A vibronic band in the actual absorption spectrum below 645 nm comes from several vibration modes,[22,32,56] which are not included in the calculation. The absorption spectrum of the reduced LHCII model without the Chl *b* manifold, used in our simulation, is calculated and shown in Figure 1 (dash-dotted green line). The spectrum is obtained (upon convolution with Gaussian distributions to account for disorder) from the stick spectra that are labelled with its major contributing pigment to the excitonic state. We list the detailed contributions of the pigments to each excitonic state in Table S1. The stick spectra are also colour-

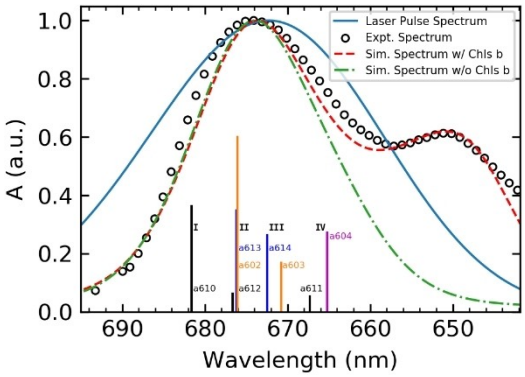

Figure 1. Calculated linear absorption spectrum of LHCII at 298 K with and without Chls *b* (dash red and dash-dotted green lines, respectively), the experimental spectrum (open circles) and a 20-fs Gaussian excitation laser pulse spectrum (solid light blue) centered at 672 nm used in the 2DES simulations. The stick spectra (vertical lines) indicate the spectral positions of the excitonic transitions labelled with its main contributing pigment. (The detailed contributions are listed in Table S1). They are also colour-coded to represent the coupled pigments that comprise an exciton group. The Roman numerals indicate the four distinct spectral components.

coded to represent the coupled pigments that comprise an exciton group. It can be seen that the excitonic states are highly overlapped in the absorption spectrum and can be grouped into four major absorption spectral components at around 682, 676, 672, and 666 nm, which have been labelled with Roman numerals I, II, III and IV, respectively. The stick spectra of LHCII with and without Chls *b* are compared in Figure S1. The removal of Chls *b* do not alter the spectral landscape much, as it can be seen that the stick spectral position differences between the two cases are no larger than 1 nm.

Simulated 2D electronic spectra for different temperatures and waiting times T_w are depicted in Figure 2. The negative amplitudes in the 2D spectra indicate the ground-state bleach and stimulated emission, while positive amplitudes indicate excited-state absorption. Three diagonal peaks emerged in the simulated 2D spectra at $T_w = 100$ fs and 77 K [Figure 2(a)], that are well separated thanks to the decrease in thermal distribution linewidth at low temperature. They correspond to the spectral components I, II, and IV as labelled in Figure 1. The diagonal signal of spectral component III at ~672 nm, which is marked with a blue filled star, is very weak compared to the other three which indicates that there is fast EET (sub-ps) from the excitons making up spectral component III to other components. With the current pigment assignment, this is possibly the rapid relaxation between two strongly coupled pigments Chl *a*614→*a*613. The result is in good agreement with the experiment[27] except for the faster timescale, since the diagonal peak (star) almost disappears in the simulation while it is relatively strong in the experiment results[27] at 100 fs.

The cross-peak at $(\lambda_\tau, \lambda_t) = (672,\ 676)$ nm, marked as a blue filled circle, reflects the downhill EET from spectral component III to II. The cross-peak at $(\lambda_\tau, \lambda_t) = (672,\ 683)$ nm, marked as a blue filled square, reflects downhill EET from spectral component III to I. Cross-peak amplitudes of the 2D spectra reflect coupling of states at $T_w =$ 0 ps and EET to probed states at longer waiting times. The weak amplitude of the cross-peak marked as a filled square reflects the weak coupling between the I and III spectral components.

Figures 2(b) and (c) show the simulated 2D spectra at $T_w =$ 3 and 10 ps, respectively. The intensity of the square marked cross-peak increased within this waiting time window indicating the slow EET from spectral component III to the lowest excitonic level, which is contributed mostly by Chl *a*610 in the model used. For spectral component IV, the diagonal peak at $(\lambda_\tau,\ \lambda_t) = (666, 666)$ nm in the simulated 2D spectra shown in Figures 2(c,f,i), exists over 10 ps which is usually described as the signal from a 'bottleneck' state in the literature.[22,29,31] The 'bottleneck' state is also observed in the experimental 2D spectra.[27] However, its decay lifetime that featured in our simulation is too long as compared to the experiment which identified it to be about 4–6 ps by a phenomenological modelling and global analysis of the experimental

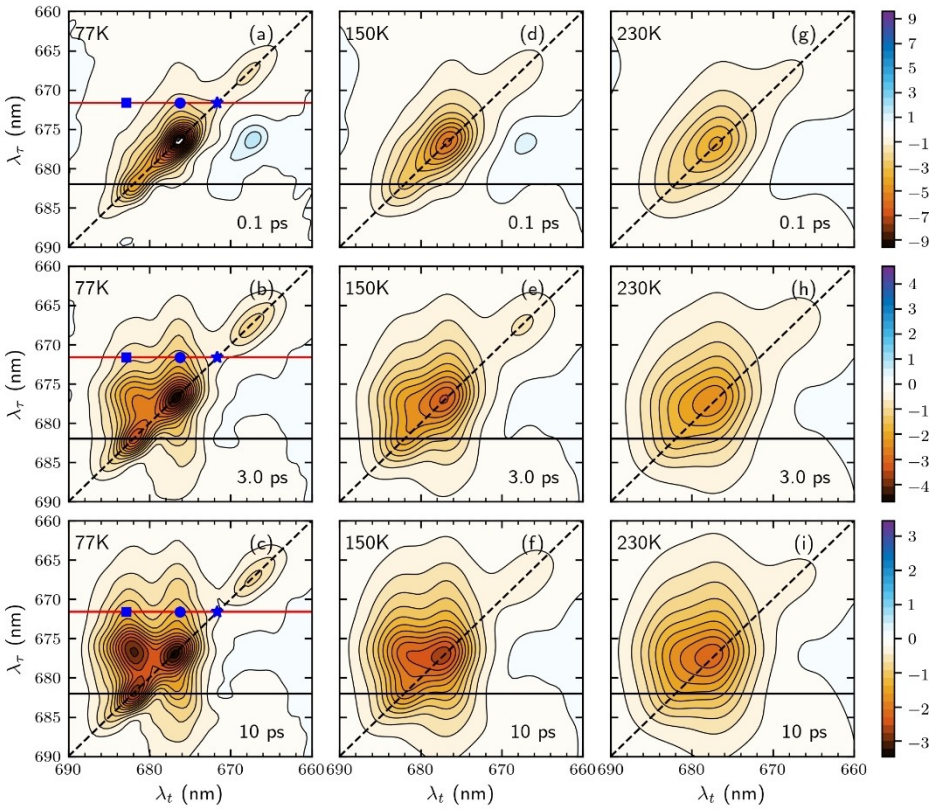

Figure 2. 2D spectra of the reduced LHCII calculated by HEOM-PMA at 77 (a–c), 150 (d–f), 230 K (g–i). From top to bottom: 2D spectra at $T_w = 100$ fs (a,d,g), 1 ps (b,e,h) and 10 ps (c,f,i). Blue filled star, circle and square represent the diagonal peak of spectral component III at ~672 nm, cross-peak at $(\lambda_\tau, \lambda_t) = (672,\ 676)$ and at $(\lambda_\tau, \lambda_t) = (672,\ 683)$ nm, respectively. The red lines indicate slices taken at 672 nm that are shown in Figure 3. The black lines indicate slices taken at 682 nm that are shown in Figure 4.

measurements.[27,57] The relatively large difference between the lifetime of the 'bottleneck' state between the simulation and experiment indicates the coupling between a604 (or any pigments contributing into the 'bottleneck' excitonic level) and other pigments is too weak in the Hamiltonian used in our current model.

To investigate the simulated EET dynamics in more detail, slices of the 2D spectra at 77 K were taken at the excitation wavelength $\lambda_\tau =$ 672 nm as shown in Figure 3(a). The waiting-time traces of the amplitudes of the marked peaks were analysed by fitting to exponential decay functions [Figure 3(b)]. The slices show that the amplitude of the diagonal peak (denoted by a star) decays with two main lifetimes, about 0.6 and 5.3 ps. On the other hand, the amplitude of the cross-peak (square) rises with two lifetimes, 1.2 and 5.4 ps. The amplitude of the cross-peak (circle) represents the intermediate EET with only one decay time of 4.8 ps. These different timescales reflect different EET pathways originating from the excitonically coupled pigments in LHCII. The 0.6-ps transfer could be attributed to the rapid relaxation between strongly coupled pigments Chl *a*614→*a*613 as mentioned above. This assignment is in good agreement with the previous phenomenological fitting results, where the time constant of 0.5 ps has been reported for this relaxation.[57] The picosecond timescales correspond to energy equilibration between the three main pigment clusters of *a*602-603, *a*613-614 and *a*610-611-612.

In order to directly visualize the extent of uphill EET and its temperature dependence, we investigate the horizontal slices of the 2D spectra along the excitation axis at $\lambda_\tau = 682$ nm at different waiting times [Figure 2(a–i)] and depict them as Figure 4 with the slices normalized at the diagonal signal at 682 nm. As Figures 4(a–c) can be seen as quasi-transient absorption spectra with narrow-band excitation at 682 nm (vertical black lines), any signal growing in the short wavelength (higher energy) region can be interpreted as uphill EET processes. In particular, the signals around 676 nm increase clearly at higher temperatures. This indicates that the 682-nm state is thermally connected with the excitons absorbing around 676 nm resulting in the enhancement of uphill energy flow at higher temperatures.

Next, we analyse and discuss the simulated data by resolving both the simulated and experimental 2D spectra into 2DDAS as explained in Sec. 2.3 and Eq. (15). There are several advantages and disadvantages associated with 2DDAS analysis, and we will briefly discuss them in the context of our studies here. The EET processes revealed by 2D spectra are inherently complex. In general, the EET processes proceed in timescales ranging from femtoseconds to tens of picoseconds. Hence the partitioning of the processes into three or four timescales may be too coarse for a thorough analysis. However, amidst the inherent complexity and large amount of information, the 2DDAS analysis does allow us to readily visualize major trends of the EET processes and is valuable for our main focus – the temperature-dependent behaviour of the EET processes. Furthermore, 2DDAS allows us to visualize more easily the donor and acceptor states, as these states can be correlated as they appear as negative and positive signals, respectively, on the

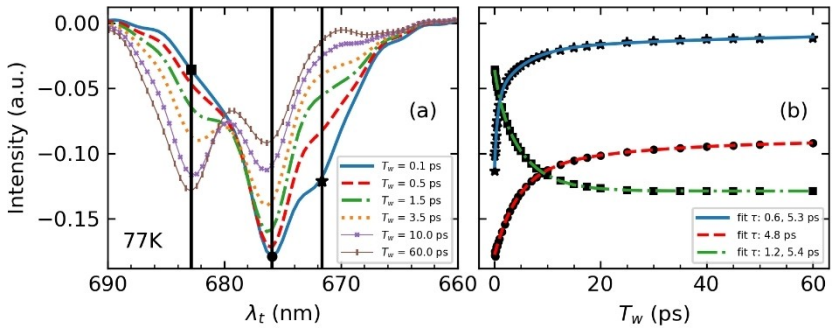

Figure 3. (a) Horizontal slices of the 2D spectra [red lines in Figure 2(a–c)] at 77 K taken at $\lambda_\tau = 672$ nm for different waiting times. (b) Peak amplitude evolution with exponential fitting in the 2D spectra corresponding to left slices at diagonal peak (672,672) nm marked as filled star, cross-peak (672,676) nm marked as filled circle and cross-peak (672,683) nm marked as filled square.

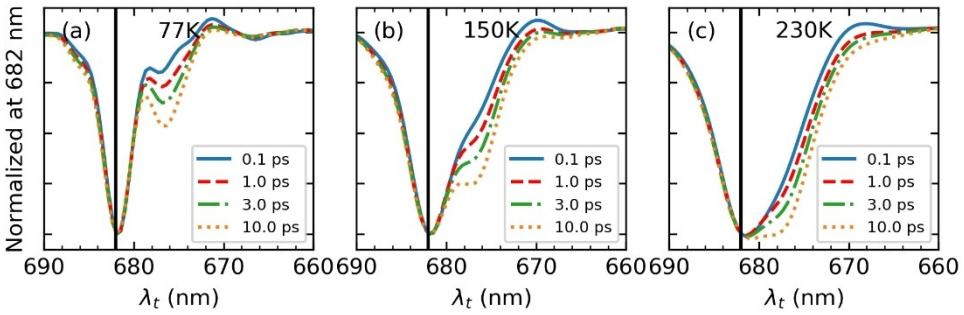

Figure 4. Horizontal slices of the 2D spectra [black lines in Figure 2(a–c)] taken at $\lambda_\tau = 682$ nm for different T_ws and temperatures. 77 (a), 150 (b), 230 K (c).

2DDAS. This is especially useful to reveal and quantify the uphill and downhill pathways associated with a given EET timescale.

Figures 5 and 6 show the 2DDAS obtained by global four-lifetime fitting that starts at $T_w = 100$ fs at temperatures 77, 150, 230 and 293 K of the simulated and experimental 2DES data, respectively. The first three 2DDAS reflect the EET processes, on three distinct timescales. The spectra show predominantly population decay of diagonal peaks and rise of

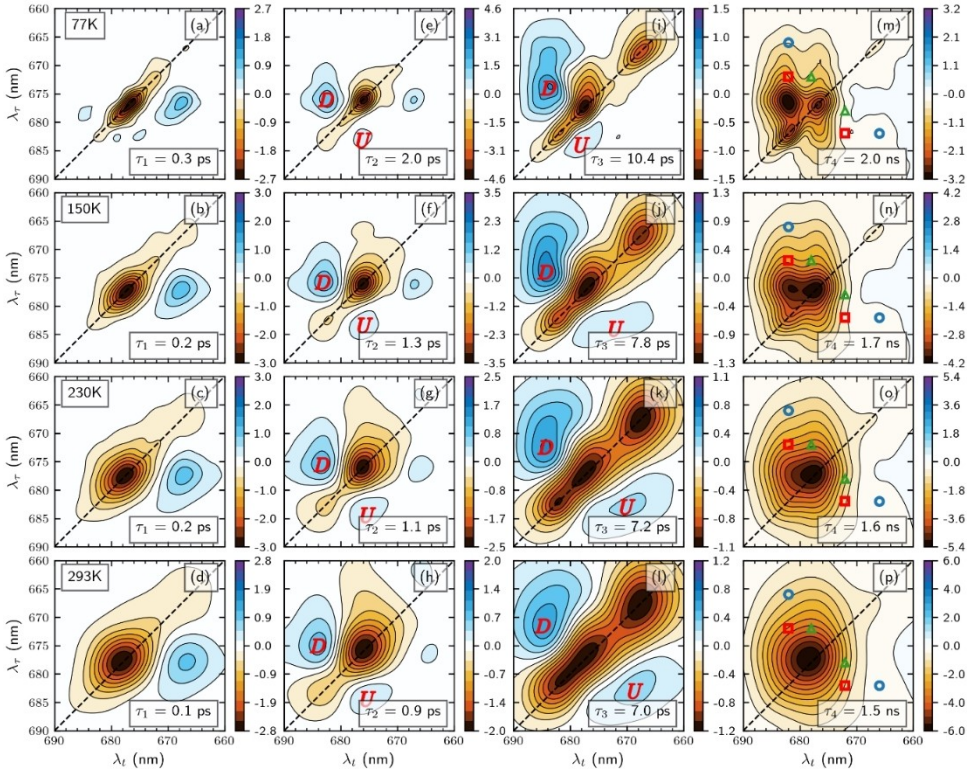

Figure 5. 2DDAS resulting from the global analysis of the simulated 2DES at 77, 150, 230 and 293 K. The respective lifetimes are indicated in the plots.

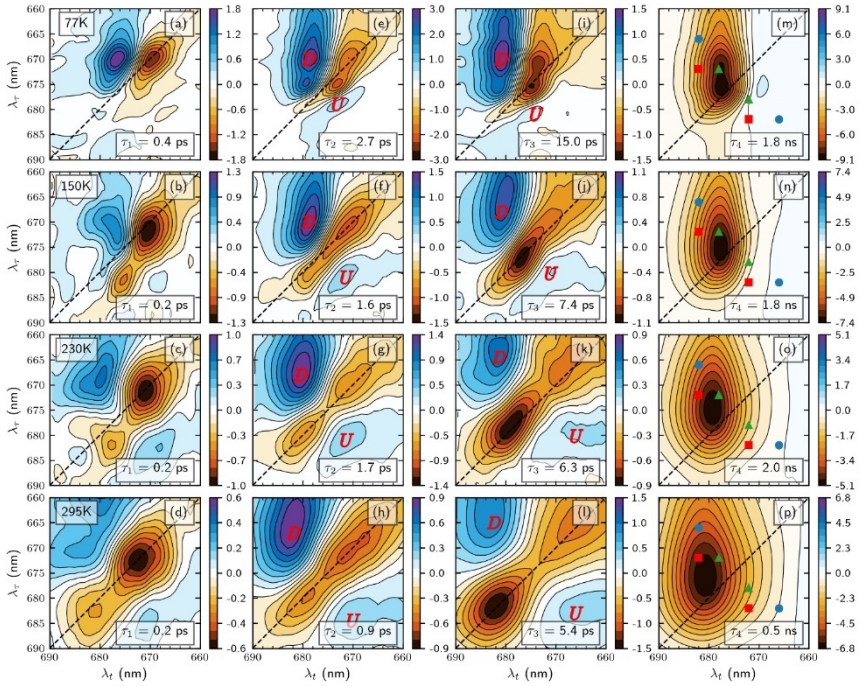

Figure 6. 2DDAS resulting from the global analysis of the experimental 2DES data at 77, 150, 230 and 295 K. Adapted with permission from Ref. [27]. Copyright 2019 American Chemical Society.

cross-peaks. The final spectrum represents the nanosecond relaxation of the equilibrated population back to the ground electronic state.

For all the temperatures studied, global analysis of the simulated and experimental data resulted in comparable decay lifetimes. The simulations reproduced a key experimental observation – the EET lifetimes generally decrease with temperature. For instance, the second and third lifetimes at 77 K – 2 and 10 ps, respectively, shortened to 0.9 and 7 ps at 293 K. For comparison, the corresponding lifetimes of the experimental data were 2.7 and 15.4 ps at 77 K and 0.9 and 5.4 ps at RT. This shows an overall trend of increasing EET rates, by the simulations. Theories such as Redfield and HEOM rely on phonon-mediated EET between excitons. Higher temperature increases the excitons access to more phonon modes, which bridges the energy gaps between excitonic states, thereby increasing the rate of EET.[28]

Comparing the simulated and experimental 2DDAS for the τ_2 timescale [Figure 5(e–h) vs. Figure 6(e–h)] and τ_3 timescale [Figure 5(i–l) vs. Figure 6(i–l)], clear similarities can be seen in terms of the temperature dependence of uphill EET. The positively-signed cross-peaks above the diagonal, reflecting downhill EET (Denoted with a '*D*'), have consistently larger amplitudes than their counterparts below the diagonal, representing uphill EET (Denoted with a '*U*'). The uphill EET is in accord with the results of the previous section as shown in Figure 4(a–c). It can also be clearly seen that the amplitudes of the cross-peaks representing uphill EET are the lowest at 77 K and increase with temperature up to 293 K, as is observed in the experiment [Figure 6(e–h) and Figure 6(i–l)] and expected from thermodynamic principles. The changes in the uphill/downhill EET ratio are also reflected in the final, nanosecond-timescale 2DDAS – at higher temperatures the simulated as well as the experimental spectra become more symmetric with respect to the diagonal line, as a result of thermalization.

There are some notable differences between the calculated and experimental EET dynamics as judged by the 2DDAS. One of such differences is found between the simulated [Figures 5(a–d)] and experimental [Figures 6(a–d)] τ_1 timescale 2DDAS. For the simulated 2DDAS, there is a prominent cross-peak of positve amplitude below the diagonal line at cross-peak $(\lambda_\tau, \lambda_t) = (676, 666)$ nm at all temperatures. The cross-peak mainly originates from biexcitonic signals made up of an exciton in the spectral component III and one from spectral component IV. This is not observed in the experiments. It could be speculated that biexcitonic annihilation processes having timescales of a few hundred femtoseconds may have rendered these coherences unobservable. On the other hand, the experimental 2DDAS has an intense positive cross-peak above the diagonal line as shown in Figure 6(a–d) $(\lambda_\tau, \lambda_t) = (670, 683)$nm which indicates a fast downhill EET process. The rapid relaxation can be seen in the simulated 2DDAS if we perform the global analysis starting from $T_w = 0$ fs, instead of $T_w = 100$ fs (Supporting Information Figure S2), which results in an additional 50-fs lifetime component. For the τ_2 timescale, the simulated 2DDAS in Figure 5(e–h) show almost no negative peaks on the upper-left centred around $(\lambda_\tau, \lambda_t) = (666, 683)$ nm compared to the experimental 2DDAS in Figure 6(e–h). One reason is that we only consider the Chl *a* manifold in the simulation, causing the simulation results to lose part of the downhill energy transfer signals from the Chl *b* manifold as compared to the experimental data. Deviations from the experiment are also observed on a picosecond timescale – especially regarding spectral component IV at ~666 nm, which relaxes mainly on a timescale of 2.7 ps in the experimental data at 77 K but the simulation shows 10 ps decay, because of overestimated lifetime of the 'bottleneck' state, as mentioned above. This also causes the EET signature centred around $(\lambda_\tau, \lambda_t) = (666, 683)$ nm, to be 'held back' and appear only in the simulated τ_3 timescale 2DDAS (Figure 5(i–l)) but not in the τ_2 timescale simulated 2DDAS (Figure 5(e–h)), as compared to the experimental spectra where the features appeared both in the τ_2 and τ_3 timescale 2DDAS. These differences in the 2DDAS are an indication that the Hamiltonian used to calculate the EET dynamics needs refinement. However, with regard to the main question of this work – whether the simulated dynamics follow the observed temperature dependence – there is a reasonable agreement with the experiment.

Built into the theoretical simulation is the detailed-balance condition[58] that ensures the ratio between the forward and backward rates in processes such as EET will follow the Boltzmann distribution function $e^{(E_a - E_b)/k_B T}$. This ratio manifests as the ratio of the amplitudes of uphill and downhill cross-peaks in the final 2DDAS as presented in Figure 7. Figures 7(a) and

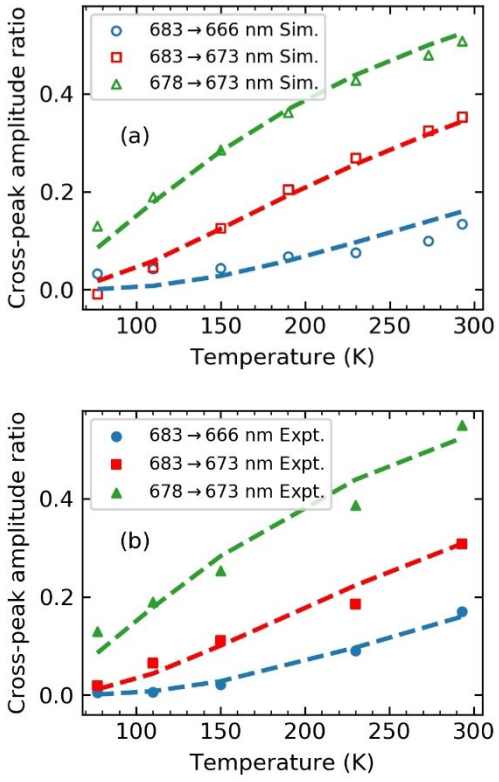

Figure 7. Temperature dependence of the uphill/downhill cross-peak amplitude ratios of the final simulated (a) and experimental (b) 2DDAS. The trend follows the Boltzmann distribution function $e^{(E_a - E_b)/k_B T}$.

7(b) present the uphill/downhill cross-peak ratios obtained from the simulated and experimental data, respectively. It can be seen in both experimental and simulated data, that the detailed balance condition, which is plotted using dashed lines, is closely followed. The small deviation between the theoretical curves and the calculated spots is due to the interference from highly congested spectral features, as well as the positive ESA signals.

Conclusion

The HEOM-PMA can describe well the EET dynamics with an appropriate model Hamiltonian. The simulated 2DES confirmed the general EET pathways in the LHCII Chl *a* manifold and gives timescales of the EET rates that are comparable with the rates measured by recent experimental 2DES studies.[27] Deviations in the relaxation rates of specific spectral components indicate that the Chl *a* part of the model Hamiltonian used needs refinement. In our simulation, the model parameters were chosen to reproduce the experimental data at room temperature initially and only the temperature parameter was varied subsequently. The simulation then deviates more from the experimental data at lower temperatures. This suggests that other parameters of the real system, for example, the spectral density, change with temperature. This is not surprising if we consider that the protein structure undergoes a phase transition over the temperature range. Therefore, further improvements can be made by utilizing temperature-dependent spectral density or static disorder[52] in the temperature-dependent spectra simulation for better comparison to the experimental results. The simulated and experimental 2D spectra were compared by subjecting the spectra to global analysis to obtain 2DDAS. This allows us to confirm that the identity of the cross-peaks on the experimental 2DES data reported recently by Akhtar et. al.[27] are correctly assigned as energy equilibration uphill and downhill EET processes. Furthermore, the temperature-dependent trend of the ratio between uphill/downhill cross-peak amplitudes is consistent with the detailed balance condition.

Acknowledgements

H.-S.T. acknowledges support from the Singapore Ministry of Education Academic Research Fund (Tier 2 MOE2015-T2-1-039 and Tier 1 RG15/18). P.H.L. acknowledges support from the Hungarian National Research, Development and Innovation Fund (grants NN-124904 and 2018-1.2.1-NKP-2018-00009). The computational work for this article was done on resources of the National Supercomputing Centre, Singapore (https://www.nscc.sg).

Conflict of Interest

The authors declare no conflict of interest.

Keywords: Light-harvesting complexes · Excitation energy transfer · Multidimensional spectroscopy · HEOM-PMA

[1] B. Green, W. Parson, *Light-Harvesting Antennas in Photosynthesis, Vol. 13*, Springer Science & Business Media **2003**.
[2] *Molecular Mechanisms of Photosynthesis*, (Ed.: R. E. Blankenship), Blackwell Science, London **2000**.
[3] Z.-F. Liu, H.-C. Yan, K.-B. Wang, T.-Y. Kuang, J.-P. Zhang, L.-L. Gui, X.-M. An, W.-R. Chang, *Nature* **2004**, *428*, 287–292.
[4] J. Standfuss, A. C. T. van Scheltinga, M. Lamborghini, W. Kühlbrandt, *EMBO J.* **2005**, *24*, 919–928.
[5] J. Connelly, M. Müller, M. Hucke, G. Gatzen, C. Mullineaux, A. Ruban, P. Horton, A. Holzwarth, *J. Phys. Chem. B* **1997**, *101*, 1902–1909.
[6] R. Agarwal, B. P. Krueger, G. D. Scholes, M. Yang, J. Yom, L. Mets, G. R. Fleming, *J. Phys. Chem. B* **2000**, *104*, 2908–2918.
[7] J. M. Salverda, M. Vengris, B. P. Krueger, G. D. Scholes, A. R. Czarnoleski, V. Novoderezhkin, H. Van Amerongen, R. Van Grondelle, *Biophys. J.* **2003**, *84*, 450–465.
[8] A. Marin, I. H. van Stokkum, V. I. Novoderezhkin, R. van Grondelle, *J. Photochem. Photobiol. A* **2012**, *234*, 91–99.
[9] J. O. Tollerud, J. A. Davis, *Prog. Quantum Electron.* **2017**, *55*, 1–34.
[10] D. M. Jonas, *Annu. Rev. Phys. Chem.* **2003**, *54*, 425–463.
[11] P. H. Lambrev, P. Akhtar, H.-S. Tan, *Biochim. Biophys. Acta Rev. Bioenerg.* **2020**, *1861*, 148050.
[12] D. Paleček, P. Edlund, S. Westenhoff, D. Zigmantas, *Am. Sci.* **2017**, *3*, e1603141.
[13] V. I. Novoderezhkin, E. Romero, J. Prior, R. van Grondelle, *Phys. Chem. Chem. Phys.* **2017**, *19*, 5195–5208.
[14] J. Dostal, T. Mančal, R.-n. Augulis, F. Vácha, J. Psencik, D. Zigmantas, *J. Am. Chem. Soc.* **2012**, *134*, 11611–11617.
[15] S. Jun, C. Yang, T. W. Kim, M. Isaji, H. Tamiaki, H. Ihee, J. Kim, *Phys. Chem. Chem. Phys.* **2015**, *17*, 17872–17879.
[16] J. Dostál, F. Vácha, J. Pšenčík, D. Zigmantas, *J. Phys. Chem. Lett.* **2014**, *5*, 1743–1747.
[17] J. C. Dean, T. Mirkovic, Z. S. Toa, D. G. Oblinsky, G. D. Scholes, *Chem* **2016**, *1*, 858–872.
[18] J. Pan, A. Gelzinis, V. Chorošajev, M. Vengris, S. S. Senlik, J.-R. Shen, L. Valkunas, D. Abramavicius, J. P. Ogilvie, *Phys. Chem. Chem. Phys.* **2017**, *19*, 15356–15367.
[19] H.-G. Duan, V. I. Prokhorenko, R. J. Cogdell, K. Ashraf, A. L. Stevens, M. Thorwart, R. D. Miller, *Proc. Natl. Acad. Sci. USA* **2017**, *114*, 8493–8498.
[20] G. D. Scholes, G. R. Fleming, L. X. Chen, A. Aspuru-Guzik, A. Buchleitner, D. F. Coker, G. S. Engel, R. Van Grondelle, A. Ishizaki, D. M. Jonas, et al., *Nature* **2017**, *543*, 647–656.
[21] J. Cao, R. J. Cogdell, D. F. Coker, H.-G. Duan, J. Hauer, U. Kleinekathöfer, T. L. C. Jansen, T. Mančal, R. J. D. Miller, J. P. Ogilvie, V. I. Prokhorenko, T. Renger, H.-S. Tan, R. Tempelaar, M. Thorwart, E. Thyrhaug, S. Westenhoff, D. Zigmantas, *Sci. Adv.* **2020**, *6*, eaaz4888.
[22] G. S. Schlau-Cohen, T. R. Calhoun, N. S. Ginsberg, E. L. Read, M. Ballottari, R. Bassi, R. van Grondelle, G. R. Fleming, *J. Phys. Chem. B* **2009**, *113*, 15352–15363.
[23] K. L. Wells, P. H. Lambrev, Z.-Y. Zhang, G. Garab, H.-S. Tan, *Phys. Chem. Chem. Phys.* **2014**, *16*, 11640–11646.
[24] H.-G. Duan, A. L. Stevens, P. Nalbach, M. Thorwart, V. I. Prokhorenko, R. D. Miller, *J. Phys. Chem. B* **2015**, *119*, 12017–12027.
[25] M. Son, A. Pinnola, R. Bassi, G. S. Schlau-Cohen, *Chem* **2019**, *5*, 575–584.
[26] P. Akhtar, C. Zhang, T. N. Do, G. Garab, P. H. Lambrev, H.-S. Tan, *J. Phys. Chem. Lett.* **2016**, *8*, 257–263.
[27] P. Akhtar, T. N. Do, P. J. Nowakowski, A. Huerta-Viga, M. F. Khyasudeen, P. H. Lambrev, H.-S. Tan, *J. Phys. Chem. B* **2019**, *123*, 6765–6775.
[28] A. Nitzan, *Chemical Dynamics in Condensed Phases*, Oxford University Press, New York **2006**.
[29] V. I. Novoderezhkin, M. A. Palacios, H. Van Amerongen, R. Van Grondelle, *J. Phys. Chem. B* **2005**, *109*, 10493–10504.
[30] V. Novoderezhkin, A. Marin, R. van Grondelle, *Phys. Chem. Chem. Phys.* **2011**, *13*, 17093–17103.
[31] T. Renger, M. Madjet, A. Knorr, F. Müh, *J. Plant Physiol.* **2011**, *168*, 1497–1509.
[32] J. Linnanto, J. Martiskainen, V. Lehtovuori, J. Ihalainen, R. Kananavicius, R. Barbato, J. Korppi-Tommola, *Photosynth. Res.* **2006**, *87*, 267–279.
[33] Y. Tanimura, R. Kubo, *J. Phys. Soc. Jpn.* **1989**, *58*, 101.
[34] A. Ishizaki, Y. Tanimura, *J. Phys. Soc. Jpn.* **2005**, *74*, 3131–3134.
[35] A. Ishizaki, G. R. Fleming, *Proc. Natl. Acad. Sci. USA* **2009**, *106*, 17255.

[36] Q. Shi, L.-P. Chen, G.-J. Nan, R.-X. Xu, Y.-J. Yan, *J. Chem. Phys.* **2009**, *130*, 084105–084108.
[37] Q. Shi, Y. Xu, Y. Yan, M. Xu, *J. Chem. Phys.* **2018**, *148*, 174102.
[38] C. Kreisbeck, T. Kramer, A. Aspuru-Guzik, *J. Chem. Theory Comput.* **2014**, *10*, 4045–4054.
[39] S. M. Bai, K. Song, Q. Shi, *J. Phys. Chem. Lett.* **2015**, *6*, 1954–1960.
[40] K. Song, S.-M. Bai, Q. Shi, *J. Chem. Phys.* **2015**, *143*, 064109.
[41] L. Seidner, G. Stock, W. Domcke, *J. Chem. Phys.* **1995**, *103*, 3998–4011.
[42] T. Kato, Y. Tanimura, *Chem. Phys. Lett.* **2001**, *341*, 329–337.
[43] M. F. Gelin, D. Egorova, W. Domcke, *J. Chem. Phys.* **2005**, *123*, 164112.
[44] Y.-C. Cheng, G. R. Fleming, *J. Phys. Chem. A* **2008**, *112*, 4254–4260.
[45] T. N. Do, M. F. Gelin, H.-S. Tan, *J. Chem. Phys.* **2017**, *147*, 144103.
[46] M. Gelin, Y. Tanimura, W. Domcke, *J. Chem. Phys.* **2013**, *139*, 214302.
[47] X. Leng, S. Yue, Y.-X. Weng, K. Song, Q. Shi, *Chem. Phys. Lett.* **2017**, *667*, 79–86.
[48] X. Leng, Y.-M. Yan, R.-D. Zhu, K. Song, Y.-X. Weng, Q. Shi, *J. Phys. Chem. B* **2018**, *122*, 4642–4652.
[49] D. Green, F. VA. Camargo, I. A. Heisler, A. G. Dijkstra, G. A. Jones, *J. Phys. Chem. A* **2018**, *122*, 6206–6213.
[50] G. Bressan, D. Green, Y. Chan, P. C. Bulman Page, G. A. Jones, S. R. Meech, I. A. Heisler, *J. Phys. Chem. A* **2018**, *123*, 1594–1601.
[51] K. Vrandecic, M. Rätsep, L. Wilk, L. Rusevich, M. Golub, M. Reppert, K.-D. Irrgang, W. Kühlbrandt, J. Pieper, *J. Phys. Chem. B* **2015**, *119*, 3920–3930.
[52] M. Golub, L. Rusevich, K.-D. Irrgang, J. Pieper, *J. Phys. Chem. B* **2018**, *122*, 7111–7121.
[53] S. Mukamel, *Principles of Nonlinear Optical Spectroscopy*, Oxford, New York **1995**.
[54] P. Hamm, M. Zanni, *Concepts and methods of 2D infrared spectroscopy*, Cambridge University Press **2011**.
[55] K. L. Wells, P. H. Lambrev, Z.-Y. Zhang, G. Garab, H.-S. Tan, *Phys. Chem. Chem. Phys.* **2014**, *16*, 11640–11646.
[56] S. Georgakopoulou, G. Van Der Zwan, R. Bassi, R. Van Grondelle, H. Van Amerongen, R. Croce, *Biochemistry* **2007**, *46*, 4745–4754.
[57] T. N. Do, A. Huerta-Viga, P. Akhtar, H. L. Nguyen, P. J. Nowakowski, M. F. Khyasudeen, P. H. Lambrev, H.-S. Tan, *J. Chem. Phys.* **2019**, *151*, 205101.
[58] W. T. Pollard, R. A. Friesner, *J. Chem. Phys.* **1994**, *100*, 5054–5065.

Manuscript received: April 11, 2020
Revised manuscript received: May 11, 2020
Accepted manuscript online: May 12, 2020
Version of record online: June 2, 2020